Electronic supplementary information

Arsenic adsorption on hematite facets: Spectroscopy and DFT study

Li Yan[†], Tingshan Chan[§], Chuanyong Jing[†,‡,*]

[†]State Key Laboratory of Environmental Chemistry and Ecotoxicology, Research Center for Eco-Environmental Sciences, Chinese Academy of Sciences, Beijing 100085, China

[‡] School of Environmental Science and Engineering, Shandong University, Qingdao 266237, China

[§]National Synchrotron Radiation Research Center, 101 Hsin-Ann Road, Hsinchu Science Park, Hsinchu 30076, Taiwan

Tel: +86 10 6284 9523; Fax: +86 10 6284 9523

E-mail: cyjing@rcees.ac.cn

Text S1. *In situ* diffuse reflectance infrared Fourier transform (DRIFT) spectroscopy. DRIFT measurement was conducted using a Thermo 6700 FTIR spectrometer equipped with diffuse reflector accessory (Harrick Scientific) and a mercury cadmium telluride (MCT) detector. Spectra were collected using 256 scans with 4 cm^{-1} resolution. Before spectra collection, a pretreatment by heating sample to 400 °C for 0.5 h under Ar flow (20 mL/min) was performed to clear surface impurities. Then the samples were cooled down to 100 °C, and the IR background spectrum was collected. After that, NH_3 flow (10 vol% NH_3/He, 10 mL/min) was filled for 60 min. Next, the gas was changed to Ar (20 mL/min), and the spectra for NH_3 desorption under Ar atmosphere were collected.

Text S2. Characterization of acid strength and heat of desorption. The strength of acid sites and heat of desorption were estimated from NH_3 temperature programmed desorption (NH_3-TPD) measurements using a Micromeritics AutoChem II 2920 chemisorption instrument. In a typical experiment, Fe_2O_3 nanocrystal was pre-treated under a flow of He to 500 °C at a heating rate of 20 °C/min to remove adsorbed water molecules. Then, NH_3 adsorption step was performed by initiating a flow of 10 vol% NH_3/He at room temperature for 60 min. Subsequently, the nanocrystal was exposed to He flow at 100 °C to remove reversibly and weakly bound NH_3 molecules from the surface. Subsequently, NH_3 desorption was carried out from 100 to 500 °C at a heating rate of 10, 5, 20, 2, 15, 7, 30, and 4 °C/min, respectively.

The heat of desorption (E_{des}) was calculated according to the following equation:[1]

$$2\ \ln Tp - 2\ln\beta = E_{des}/RTp + B$$

where Tp is the temperature (K) at maximum desorption rate; β is the heating rate; R is the gas constant [R=8.314 J/(mol·K)]; and *B* is the intercept.

Text S3. *In situ* flow cell ATR-FTIR study. The *in situ* flow cell ATR-FTIR measurements were performed using a Thermo-Nicolet iS50R FTIR spectrometer equipped with a horizontal attenuated total reflectance (HATR) cell (PIKE Tech) and a liquid-nitrogen-cooled mercury-cadmium-telluride (MCT) detector. In a typical experiment, a 0.5 mL of the adsorbent suspension (4.0 g/L) was spread on the ZnSe crystal and air-dried at room temperature. To remove the loosely deposited particles and other impurities on the surface of the coated film, a 0.04 M NaCl solution at pH 7 was used to rinse the surface at a rate of 0.5 mL/min until there was no further change in the IR spectra (about 2 h). A background spectrum consisted of the adsorbance of the coated film and ZnSe crystal was collected and saved. Then 50 or 500 mg/L As(III/V) in 0.04 M NaCl solution were passed through the flow cell at pH 7. Spectra in the range of 4000 to 650 cm^{-1} were collected with a time increment of 10 min until the adsorption reached equilibrium (about 3 h). All solutions were purged with N_2 in the dark during the spectra collection process.

The Omnic 9.2 software (Thermo Fisher Scientific Inc.,USA) was used to collect and analyze the spectra, including subtraction, normalization, and baseline correction. Deconvolution of the spectra was performed using the Peak-Fit software package (Systat Software Inc.). Second-derivative spectra were calculated to determine the number and centroid positions of contributing bands. The experimental spectra were then fitted by optimizing the amplitudes and the widths of the Gaussian functions, and the width of each band was consistent in all fitting.[2]

To confirm the peak shift upon deprotonation, FTIR spectra of As(III/V) solutions in the absence of hematite-coated interface was performed at varied pH conditions. In the experiment, 40 mM As(III/V) solutions were spread on the ZnSe crystal, and the spectra were collected under similar conditions with that in the presence of hematite-coated interface.

Text S4. EXAFS study. EXAFS spectroscopy was employed to characterize the local coordination environment of adsorbed As(III/V) on Fe_2O_3 facets. The samples for EXAFS study were prepared by reacting 50 mg/L As(III/V) with 1 g/L Fe_2O_3 in 0.04 M NaCl solution at pH 7. After the suspensions were reacted for 24 h, the solid-liquid was separated by centrifugation and the wet paste was freeze-dried. The powdered sample was sealed between two layers of Kapton tape for EXAFS measurements.

The As K-edge spectra (11,867 eV) were collected on beamline 01C1 at the National Synchrotron Radiation Research Center (NSRRC), Taiwan. The spectra were collected in fluorescence mode using a standard Lytle detector, and acquired at cryogenic temperature (about 85 K) using a helium cryostat to prevent beam-induced oxidation. To eliminate the effect of Fe fluorescence, germanium (Ge) filter was added before Lytle detector. Monochromatic X-rays were produced with a Si(111) double crystal monochromator with an intrinsic resolution $\Delta E/E$ of 1.4×10^{-4}. The beam size was adjusted to 2 mm×1 mm. The energy calibration of the monochromator was checked by a Au foil (first maximum of the first derivative of the Au L_3-edge XANES spectrum at 11,919 eV). The scans for EXAFS data started at 11,667 eV using a step size of 10 eV. Across the edge the step size was reduced to 0.6 eV. The EXAFS was collected with a resolution of 0.06 $Å^{-1}$ in *k*-space. Multiple scans were collected for each sample to improve the signal-to-noise ratio, and the spectra were inspected for overall quality, and averaged.

Text S5. DFT calculations. Periodic DFT calculations were performed with VASP 5.4 package. The bulk unit cell of hematite (α-Fe_2O_3) was first geometry-optimized, resulting in a lattice parameters of a=b=5.035 Å and c=13.720 Å, which were in good agreement with experiment (a=b=5.036 Å and c=13.749 Å, JCPDS No. 33-0664), and other DFT calculations.[3] Hematite {001}, {110}, and {214} facets were cleved from the optimized bulk structure, and a neutrally-charged 2×2 supercell with $Fe_{32}O_{48}$ for {001} slab, 1×2 supercell with $Fe_{32}O_{48}$ for {110} slab, and 1×2 supercell with $Fe_{48}O_{72}$ for {214} slab were built. A vacuum slab of 20 Å was added to separate each slab in the direction along the surface normal. The lattice parameters were as follows: for {001} facet, a = b = 10.07 Å, c = 28.55 Å, α = β = 90°, γ = 120°; for {110} facet, a = 7.40 Å, b = 10.84 Å, c = 29.57 Å, α = β = 90°, γ = 95.7°; for {214} facet, a = 12.49 Å, b = 10.84 Å, c = 28.62 Å, α = β = 90°, γ = 86.6°. Full geometry optimization was carried out with no imposed symmetry on the entire slab, with structural convergence set to a force tolerance of 0.05 eV/Å and an energy tolerance of 1.0×10^{-5} eV. K-points of 3×3×1 for {001}, 3×2×1 for {110}, and 3×2×1 for {214} facet, respectively, were modeled using a Monkhorst–Pack mesh. Electrostatically neutral H_3AsO_3 and H_3AsO_4 molecules were independently geometry-optimized in a periodic box of 10 Å side-lengths, and then was added to the optimized {001}, {110}, and {214} facets to build the adsorption structures.

DFT calculations were carried out using the generalized gradient approximation (GGA) approach of Perdew-Burke-Ernzerhof (PBE) for the exchange-correlation energy calculation.[4] The energy cutoff was set to 400 eV. On-site Coulomb potential (DFT+U) correction was applied to the 3d electron of Fe atoms with U=5.0 eV. Hematite exhibits an antiferromagnetic ground state, with alternating double layers of spin-up and spin-down electrons perpendicular to c-axis.[5] To model the antiferromagnetic configuration of hematite, spin-polarized calculations were carried out with high spin state ($S = 5/2$) identified as the most stable configuration.[6] Electronic structure analysis was performed with the LOBSTER 3.2 program.[7] The partial density of states (PDOS) and crystal orbital Hamilton populations (COHP) were used to analyze bonding chemistry of surface complexes.[8, 9] The PDOS plots provide information on the partial electron density distribution of a particular atomic orbital. The COHP densities give the electron density distribution of bonding and antibonding orbital fragments. The negative contributions of COHP (−COHP) were plotted, and the positive/negative peaks in the plots indicate the bonding/antibonding interaction regimes. All the figures were plotted with the Fermi level set as the reference point at 0 eV.[6]

The surface energy (γ) of each facet was calculated as following equation:

$$\gamma = \frac{E_{slab} - NE_{bulk}}{2A}$$

where E_{slab} is the total energy of the slab, E_{bulk} is the energy per unit of Fe_2O_3, N is the total number of Fe_2O_3 units contained in the slab model, and A is the surface area of slab.

The surface energy (γ) of hydrated surface was calculated as following equation:

$$\gamma = \frac{E_{slab} - NE_{bulk} - 8E_{molecule}}{2A}$$

where E_{slab} is the total energy of the slab, E_{bulk} is the energy per unit of Fe_2O_3, $E_{molecule}$ is the energy of one water molecule, *N* is the total number of Fe_2O_3 units contained in the slab model, and *A* is the surface area of slab.

The adsorption energy (E_{ads}) in eV for surface complex was calculated according to the following equation:[10]

$$E_{ads} = E_{molecule+slab} - (E_{slab} + E_{molecule})$$

where $E_{molecule+slab}$ is the total energy of the surface complexes, and E_{slab} and $E_{molecule}$ represent the energy of surface and adsorbed molecule, respectively.

Text S6. Surface terminations.

The surface terminations were chosen based on the surface energy calculation, because according to Wulff's construction rule, crystal facets emerge from the thermodynamically-favored growth of facet with the lowest surface energy.[11, 12] The layers with distinct terminations in the slab were numbered by sequence order beginning at the topmost layer.

As shown in Fig. S1 and Table S1, the single Fe layer termination on the {001} facet is most thermodynamically stable with surface energy (γ) of 1.63 J/m^2. On the {110} facet, the most stable surface is terminated by five-fold coordinated Fe with γ of 1.32 J/m^2. Our calculated surface energies of the {001} and {110} facets are consistent with previous report, which suggested γ values of 1.4 J/m^2 for {001} facet and 1.2 J/m^2 for {110} facet, respectively.[13] On high-index {214} facet, the most stable surface is terminated by mixed Fe_{5c}, Fe_{4c}, and Fe_{3c} sites, and highly relaxed surface configuration show a γ value of 1.77 J/m^2 (Layer 2 in Fig. S1). Surface termination with the lowest surface energy is the representative surface in the aqueous systems. Although the ideal structural modes may not completely represent the naturally occurring Fe_2O_3–water interfaces, they provide a well-defined starting point to characterize the facet-dependent adsorption. This protocol is widely followed to investigate the solid-water interfacial adsorption mechanism in previous studies.[13-16]

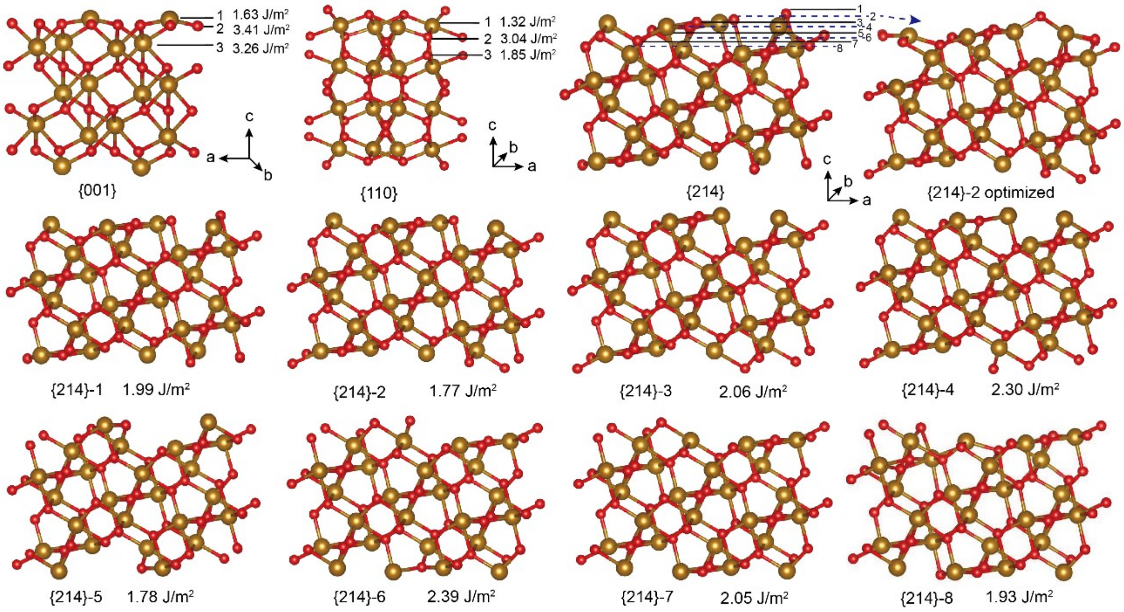

Fig. S1. Surface structures of Fe_2O_3 facets with atomic layering sequence.

Table S1. DFT calculated surface energy (γ) of Fe_2O_3 facets with distinct terminations.

Facets	Termination	E_{slab} (eV)	E_{bulk} (eV)	A (Å^2)	γ (J/m^2)
{001}	Layer-1	-514.22	-199.53 ($Fe_{12}O_{18}$)	87.82	1.63
$Fe_{32}O_{48}$	Layer-2	-494.69			3.41
	Layer-3	-496.41			3.26
{110}	Layer-1	-518.95	-199.53 ($Fe_{12}O_{18}$)	79.81	1.32
$Fe_{32}O_{48}$	Layer-2	-501.82			3.04
	Layer-3	-513.69			1.85
{214}	Layer-1	-764.62	-199.53 ($Fe_{12}O_{18}$)	135.18	1.99
$Fe_{48}O_{72}$	Layer-2	-768.32			1.77
	Layer-3	-763.42			2.06
	Layer-4	-759.24			2.30
	Layer-5	-768.09			1.78
	Layer-6	-757.88			2.39
	Layer-7	-763.60			2.05
	Layer-8	-765.56			1.93

Text S7. Raman spectra and surface structure.

Raman spectra show that the relative intensity of E_g peaks was lowest for {110} nanorod, but highest for {001} nanoplate, suggesting different atomic structures and O–Fe–O vibration modes on each facet (Fig. S2). A_{1g} peaks are attributed to antisymmetric stretching and bending vibrations of O–Fe–O in Fe_2O_3, and E_g peaks are ascribed to the symmetric vibration modes of O–Fe–O.[17] On {001} facet, the bonding modes are three-coordinated 3c-Fe and 3c-O (Fig. 1h). Due to the C_{3v} symmetry of O–Fe–O bond by coordinating 3c-Fe with 3c-O, the number of the symmetric vibration modes of O–Fe–O was increased in the presence of {001} facet, and thus the intensity of the E_g peaks in Raman spectra was increased. On {110} facet, 5c-Fe, 3c-O, and 2c-O bonding modes are distributed on the surface; due to the large number of unsaturated 5c-Fe, the number of antisymmetric vibration modes of O–Fe–O become obvious, and the intensity of the A_{1g} peaks become increased. On {214} facet, complex bonding modes of 5c-Fe, 4c-Fe, 3c-Fe, 3c-O, and 2c-O were observed; thus, the intensities of the A_{1g} and E_g peaks are compromised when compared to those on {001} and {110} facets.

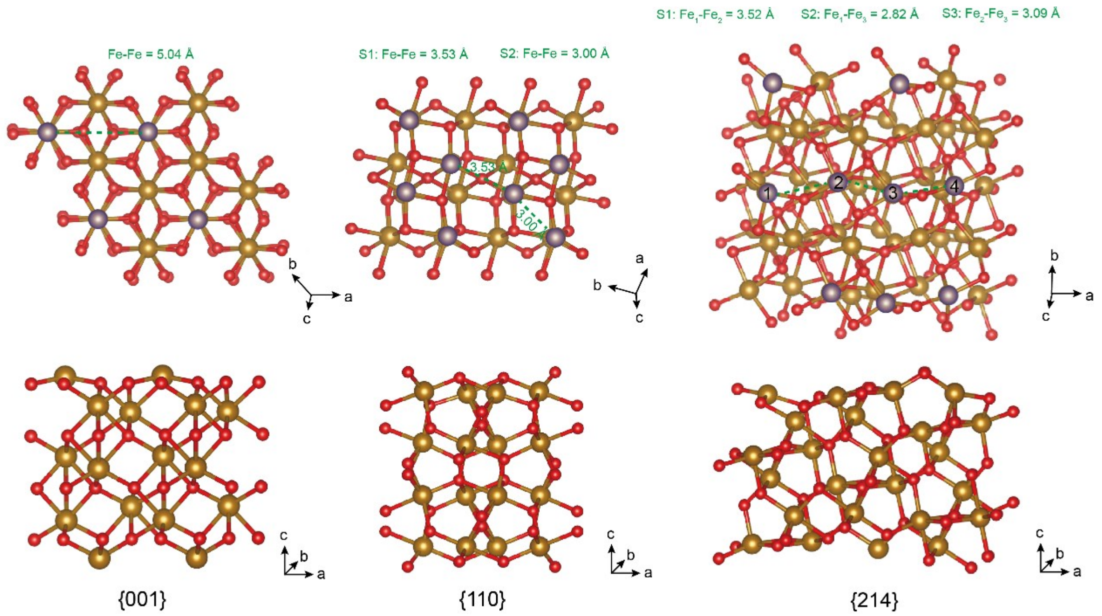

Fig. S2. The top view and corresponding side view of atomic arrangement on Fe_2O_3 {001}, {110}, and {214} facets. The red, purple, and brown spheres represent O, under-coordinated Fe, and bulk Fe atoms, respectively. Under-coordinated Fe atoms on the {001} facet are three-coordinated Fe_{3c} sites, and under-coordinated Fe atoms on the {110} facet are five-coordinated Fe_{5c} sites. On the {214} facet, numbered (1, 2, 3, and 4) purple spheres presented three-coordinated Fe_{3c} site, five-coordinated Fe_{5c} site, and two types of four-coordinated Fe sites (Fe_{4c}-1 and Fe_{4c}-2).

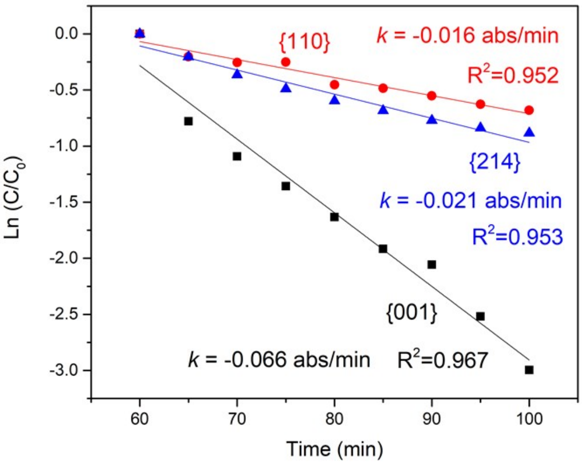

Fig. S3. Pseudo-first order kinetics model simulation for NH_3 desorption on the {001}, {110}, and {214} facets.

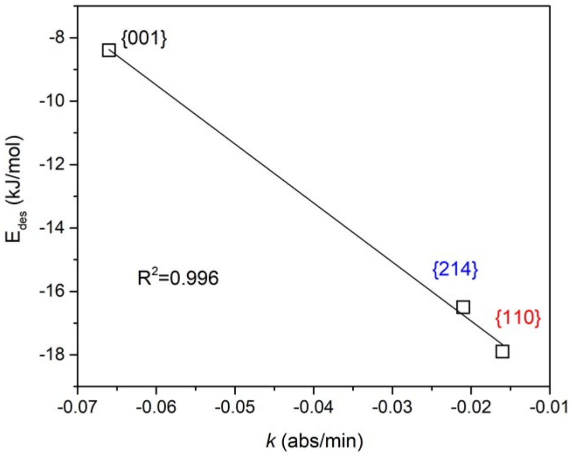

Fig. S4. The linear relationship of heat of desorption with NH_3 desorption rate.

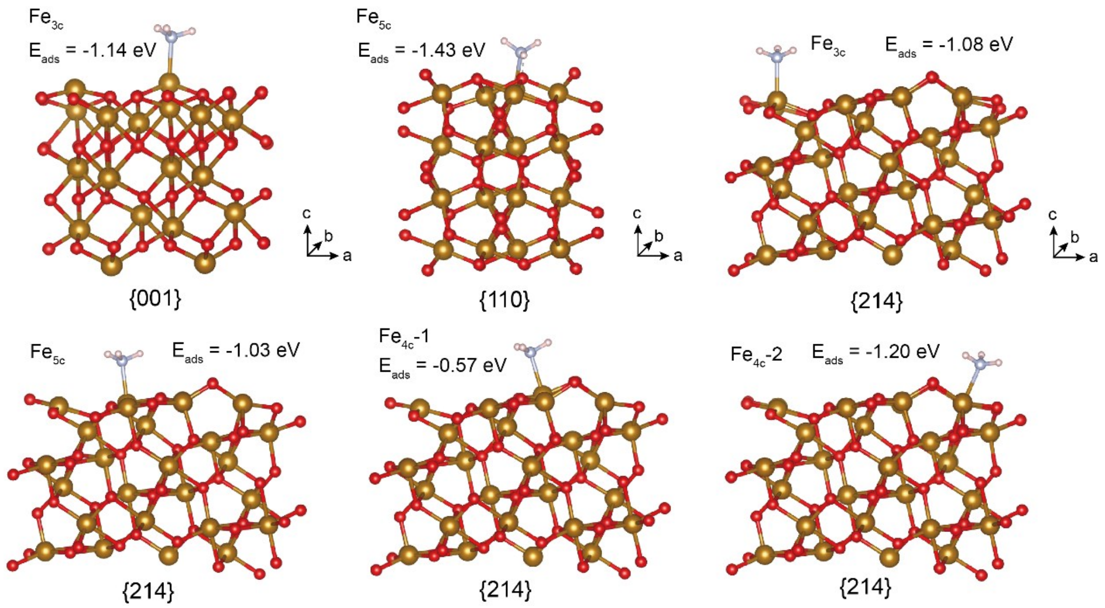

Fig. S5. DFT-optimized NH_3 adsorption configurations at different sites on the {001}, {110}, and {214} facets, the E_{ads} was calculated in Table S2.

Table S2. NH_3 adsorption energies (eV) on Fe_2O_3 {001}, {110}, and {214} facets.

Facet	Site	NH_3+slab	Slab	NH_3	E_{ads}
{001}	Fe_{3c}	-534.87	-514.22	-19.51	-1.14
{110}	Fe_{5c}	-539.89	-518.95	-19.51	-1.43
{214}	Fe_{3c}	-788.91	-768.32	-19.51	-1.08
	Fe_{5c}	-788.86	-768.32	-19.51	-1.03
	Fe_{4c}-1	-788.40	-768.32	-19.51	-0.57
	Fe_{4c}-2	-789.04	-768.32	-19.51	-1.20

Table S3. Summary of As(III/V) adsorption on hematite.

Hematite	BET (m^2/g)	pHpzc	As concentration (mg/L)	pH	Adsorbent (g/L)	Adsorption capacity (mg/g)	Surface loading (mg/m^2)	Ref
Flower like α-Fe_2O_3	130		$[As(V)]_0$ = 10-200	3	0.4	51	0.392	18
3D flowerlike α-Fe_2O_3	40		$[As(V)]_0$ = 0-10.63	4	2	7.6	0.190	19
Hollow Nestlike α-Fe_2O_3	152.42		$[As(V)]_0$ = 0-500		0.5	75.3	0.494	20
Porous hematite	73.458	6.0	$[As(III)]_e$ = 0-12	6	1	14.46	0.197	21
Porous hematite	93	6.8	$[As(V)]_0$ = 2-45	7	1	8.94	0.096	22
Porous hematite	3.75		$[As(v)]_e$ = 0-15	5	30	0.65	0.173	23
Portland cement-porous hematite	22.86		$[As(III)]_e$ = 0-21	7	1	9.84	0.430	24
Iron oxide nanoparticles	11.47	9.6	$[As(V)]_0$ = 0.1-2	6	2	2.325	0.203	25
Synthetic hematite	76.25		$[As(III)]_0$ = 2-150	9	0.2	109.89	1.441	26
	76.25		$[As(V)]_0$ = 2-150	3	0.2	181.82	2.385	
Synthetic hematite	162		$[As(III)]_0$ = 0-200	7	0.02-0.06	95	0.586	27
	162		$[As(V)]_0$ = 0-200	7	0.02-0.06	47	0.290	
α-Fe_2O_3/diatomite	30		$[As(III)]_0$ = 5-90	3.5	0.4	60.65	2.022	28
	30		$[As(V)]_0$ = 5-90	3.5	0.4	81.16	2.705	
Synthetic α-Fe_2O_3	22.5		$[As(III)]_e$ = 0-4.5	4	1	4.217	0.187	29
Natural hematite	0.381		$[As(III)]_e$ = 0-37.5	7.3		0.27	0.698	30
	0.381		$[As(V)]_e$ = 0-37.5	7.3		0.83	2.175	
Natural hematite	14.4	7.1	$[As(V)]_0$ = 1-10	4.2	40	0.2188	0.015	31
Natural hematite		6.5	$[As(III)]_0$ = 0.025-0.5	6.5	0.1	1.94		32
Natural hematite	3.77	6.5	$[As(V)]_0$ = 5-50	5	5	0.752	0.200	33
Commercial hematite	5.05		$[As(V)]_0$ =0.6	5-9	0.05-1	0.47-0.66	0.093-0.131	34
Commercial hematite	1.66	8.1	$[As(V)]_0$ = 0.075-15	6	4	0.412	0.248	35
Commercial Fe_2O_3	50		$[As(III)]_0$ = 0.01-2	6.8-8	0.01	2.899	0.058	36
	50		$[As(V)]_0$ = 0.01-2	6.8-8	0.01	4.122	0.082	
Commercial Fe_2O_3	4.159		$[As(III)]_e$ = 0-35	7	1	0.845	0.203	37
Hematite			$[As(III)]_0$ = 1-135	7	0.42	32.80		38

{001} Fe_2O_3	4.7	$[As(III)]_0$ = 1-200	7	1	5.9	1.26	This work
	4.7	$[As(V)]_0$ = 1-200	7	1	4.0	0.85	
{110} Fe_2O_3	17.9	$[As(III)]_0$ = 1-200	7	1	7.7	0.43	
	17.9	$[As(V)]_0$ = 1-200	7	1	4.9	0.27	
{214} Fe_2O_3	18.9	$[As(III)]_0$ = 1-200	7	1	8.3	0.44	
	18.9	$[As(V)]_0$ = 1-200	7	1	5.9	0.31	

Text S8. ATR-FTIR study.

The IR spectra of dissolved As(III) and As(V) were derived by subtracting the spectrum of deionized water. The first and second pKa values for As(III) are relatively high ($pK_{a,1}$ = 9.2 and $pK_{a,2}$ = 12.7, Fig. S7a), indicating that the fully protonated $As(OH)_3$ species should be the predominant species at pH < 9. Fig. S7b reveals a broad band centered at 765 cm^{-1} ascribed to As–(OH) vibrations at pH 4.97. At pH 10.81 with dominant $H_2AsO_3^-$ species, a broad band at 810 cm^{-1} was observed, indicating the peak shift to high frequency upon As–OH deprotonation. Therefore, the peak shift from 709 cm^{-1} to 790 cm^{-1} for adsorbed As(III) can be ascribed to the deprotonation of As–OH upon adsorption.

Four protonation states of As(V) include H_3AsO_4, $H_2AsO_4^-$, $HAsO_4^{2-}$, and AsO_4^{3-} with corresponding pKa values at 2.3, 6.8, and 11.6 (Fig. S7c). Fig. S7d presents the FTIR spectra of dissolved As(V) recorded at different pH values. At pH=2.44, the dominant species in solution are H_3AsO_4 (39%) and $H_2AsO_4^-$ (61%), showing two IR active modes for the symmetric and asymmetric As–O stretches at 878 cm^{-1} and 908 cm^{-1}.[2] These frequencies remain unchanged upon increasing the pH to 4.92 with dominant $H_2AsO_4^-$ (100%), verifying that neither mode arises from the fully protonated H_3AsO_4. At pH=7.47, the dominant species in solution are $HAsO_4^{2-}$ (76%) and $H_2AsO_4^-$ (24%), and the asymmetric As–O stretch in $HAsO_4^{2-}$ gives rise to a strong, signature vibrational band at 858 cm^{-1}, in good agreement with previous results.[2, 39] The peak at 858 cm^{-1} persists at pH range of 9.03-10.45, and a new band is observed at 809 cm^{-1}, which can be assigned to the As–O vibrations for the totally deprotonated AsO_4^{3-}.[42]

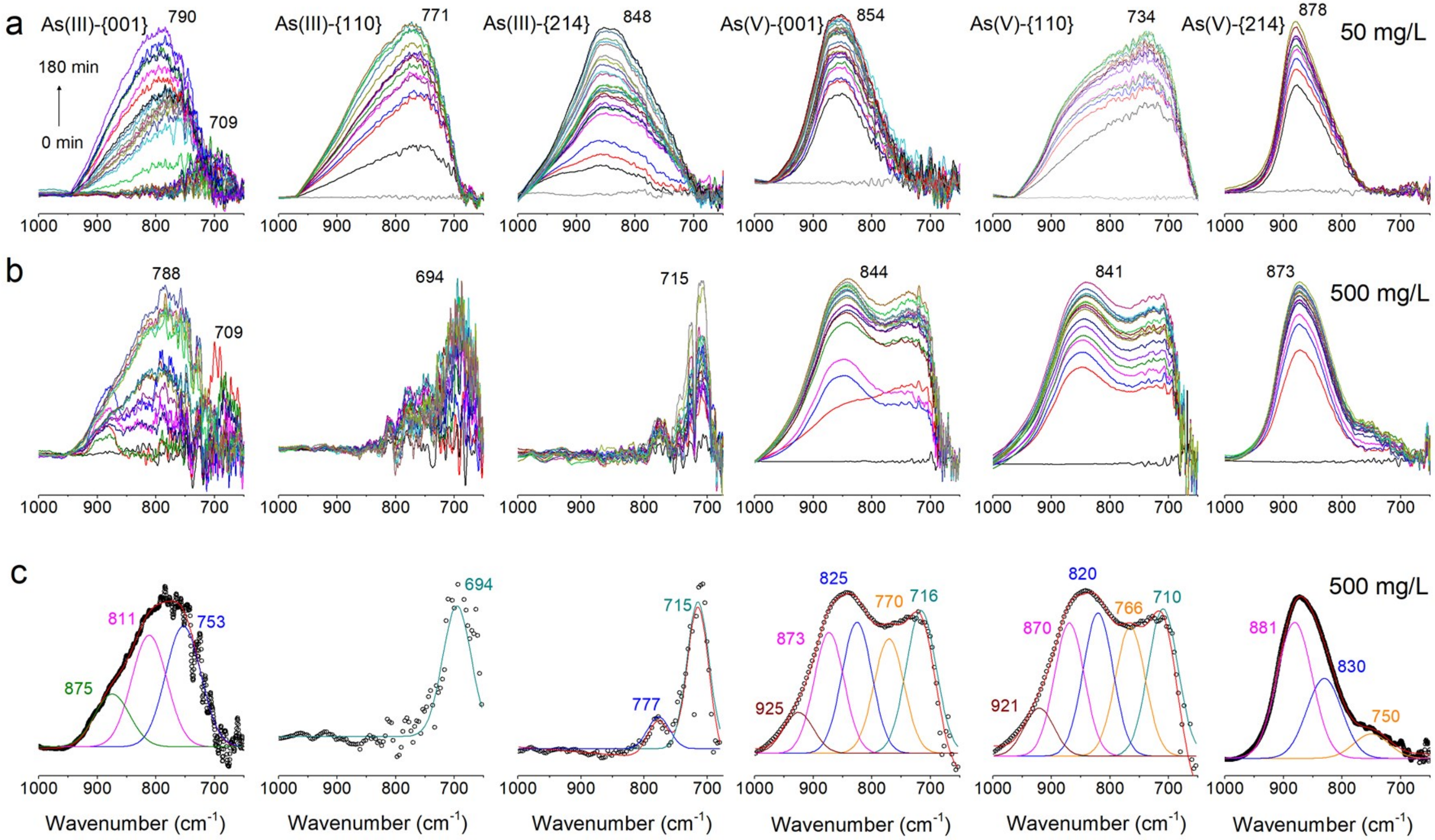

Fig. S6. ATR-FTIR spectra of (a) 50 mg/L and (b) 500 mg/L As(III/V) adsorption on Fe$_2$O$_3$ {001}, {110}, and {214} facets with increasing time at pH 7. (c) Observed (circles) and peak fitting results (lines) for 500 mg/L As(III/V) adsorption. The peak assignment is presented in Table S5.

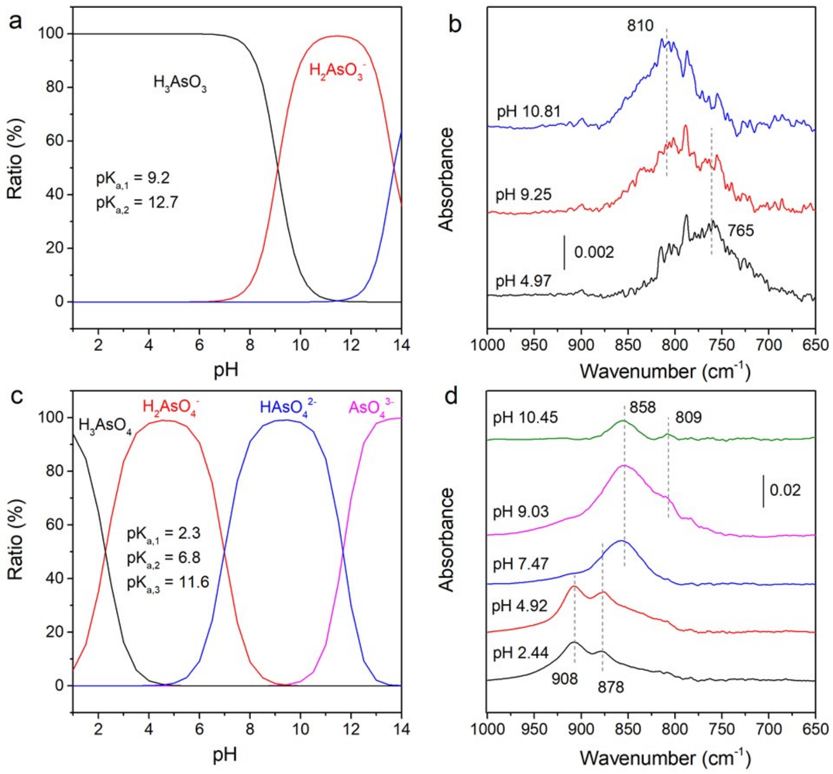

Fig. S7. (a) As(III) and (c) As(V) species calculated in MINTEQ software. FTIR spectra of 40 mM (b) As(III) and (d) As(V) solutions recorded at different pH conditions.

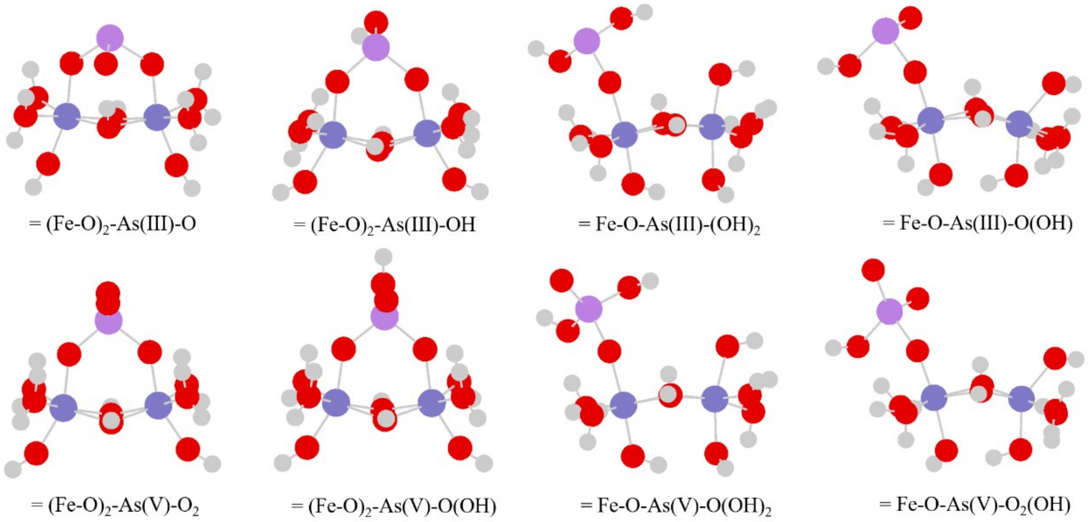

≡(Fe-O)$_2$-As(III)-O ≡(Fe-O)$_2$-As(III)-OH ≡Fe-O-As(III)-(OH)$_2$ ≡Fe-O-As(III)-O(OH)

≡(Fe-O)$_2$-As(V)-O$_2$ ≡(Fe-O)$_2$-As(V)-O(OH) ≡Fe-O-As(V)-O(OH)$_2$ ≡Fe-O-As(V)-O$_2$(OH)

Fig. S8. As(III) and As(V) surface complexes for IR spectra calculation. Fe: blue, O: red, As: purple, H: grey.

Table S4. Peak fit and calculated modes of IR spectra for 50 mg/L As(III/V) adsorption on Fe_2O_3 facets.

Color in Figure 4	Peak position (cm^{-1})	Peak area (%)	Assignment	Calculated position (cm^{-1})
{001}-As(III)				
Blue	767	39.8	ν_s As-OFe = Fe-O-As(III)-$(OH)_2$	761
Magenta	821	38.1	ν As-OH = Fe-O-As(III)-$(OH)_2$	821
Olive	878	22.2	ν As-O = Fe-O-As(III)-$(OH)_2$	855
{110}-As(III)				
Blue	743	31.7	ν_s As-OFe = $(Fe\text{-}O)_2$-As(III)-O	742
Magenta	794	31.4	ν_s As-OFe = $(Fe\text{-}O)_2$-As(III)-OH	794
Olive	849	25.2	ν_{as} As-O = $(Fe\text{-}O)_2$-As(III)-O	871
Wine	906	11.7	ν Fe-O = $(Fe\text{-}O)_2$-As(III)-OH	900
{214}-As(III)				
Blue	750	16.0	ν_s As-OFe = $(Fe\text{-}O)_2$-As(III)-O	742
Magenta	805	27.7	ν_s As-OFe = $(Fe\text{-}O)_2$-As(III)-OH	794
Olive	856	33.8	ν_{as} As-O = $(Fe\text{-}O)_2$-As(III)-O	871
Wine	901	15.5	ν Fe-O = $(Fe\text{-}O)_2$-As(III)-OH	900
Dark yellow	943	7.0	ν Fe-O = $(Fe\text{-}O)_2$-As(III)-OH	945
{001}-As(V)				
Blue	791	18.8	ν_s As-OFe = Fe-O-As(V)-O_2(OH)	789
Magenta	844	50.1	ν_{as} As-O = Fe-O-As(V)-O_2(OH)	833
Wine	892	31.2	ν Fe-O = Fe-O-As(V)-O_2(OH)	913
{110}-As(V)				
Dark cyan	704	24.2	ν_s As-OH = $(Fe\text{-}O)_2$-As(V)-O(OH)	712
Organe	752	24.9	ν_s As-OFe = $(Fe\text{-}O)_2$-As(V)-O_2	745
Blue	803	22.3	ν_s As-OFe = $(Fe\text{-}O)_2$-As(V)-O(OH)	818
Magenta	859	18.0	ν_{as} As-O = $(Fe\text{-}O)_2$-As(V)-O(OH)	860
Wine	900	10.5	ν Fe-O = $(Fe\text{-}O)_2$-As(V)-O(OH)	905
{214}-As(V)				
Blue	821	30.2	ν_s As-OFe = $(Fe\text{-}O)_2$-As(V)-O(OH)	818
Magenta	879	69.8	ν_{as} As-O = $(Fe\text{-}O)_2$-As(V)-O(OH)	860

Table S5. Peak fit and calculated modes of IR spectra for 500 mg/L As(III/V) adsorption on Fe_2O_3 facets.

Color in Figure 4	Peak position (cm^{-1})	Peak area (%)	Assignment	Calculated position (cm^{-1})
{001}-As(III)				
Blue	753	42.3	ν_s As-OFe = Fe-O-As(III)-$(OH)_2$	761
Magenta	811	39.1	ν As-OH = Fe-O-As(III)-$(OH)_2$	821
Olive	875	18.5	ν As-O = Fe-O-As(III)-$(OH)_2$	855
{110}-As(III)				
Dark cyan	694	100	ν_s As-OH = $(Fe\text{-}O)_2$-As(III)-OH	693
{214}-As(III)				
Dark cyan	715	80.5	ν_s As-OH = $(Fe\text{-}O)_2$-As(III)-OH	693
Blue	777	19.5	ν_s As-OFe = $(Fe\text{-}O)_2$-As(III)-OH	794
{001}-As(V)				
Dark cyan	716	25.9	ν_s As-OH = Fe-O-As(V)-O$(OH)_2$	715
Orange	771	20.8	ν_s As-OFe = Fe-O-As(V)-O_2(OH)	789
Blue	825	23.8	ν_s As-OFe = Fe-O-As(V)-O$(OH)_2$	819
Magenta	873	22.0	ν_{as} As-O = Fe-O-As(V)-O$(OH)_2$	853
Wine	925	7.4	ν Fe-O = Fe-O-As(V)-O$(OH)_2$	936
{110}-As(V)				
Dark cyan	710	26.4	ν_s As-OH = $(Fe\text{-}O)_2$-As(V)-O(OH)	712
Organe	766	20.9	ν_s As-OFe = $(Fe\text{-}O)_2$-As(V)-O_2	745
Blue	820	23.2	ν_s As-OFe = $(Fe\text{-}O)_2$-As(V)-O(OH)	818
Magenta	870	21.6	ν_{as} As-O = $(Fe\text{-}O)_2$-As(V)-O(OH)	860
Wine	921	7.8	ν Fe-O = $(Fe\text{-}O)_2$-As(V)-O(OH)	905
{214}-As(V)				
Orange	750	10.2	ν_s As-OFe = $(Fe\text{-}O)_2$-As(V)-O_2	745
Blue	830	33.3	ν_s As-OFe = $(Fe\text{-}O)_2$-As(V)-O(OH)	818
Magenta	881	56.6	ν_{as} As-O = $(Fe\text{-}O)_2$-As(V)-O(OH)	860

Text S9. Identification of surface active site for As(III/V) adsorption by DFT calculations.

DFT-optimized As(III/V) adsorption configurations on bare facets are shown in Fig. S9, and the E_{ads} was calcuated in Table S6. Specifically, ^{1}V geometry of As(III/V) complex was observed on the {001} facet, due to a large distance of 5.04 Å for adjacent Fe atoms (Fig. S2).[14] The E_{ads} values for As(III) and As(V) adsorption on the {001} facet were comparable (-1.49 eV, Table S6). Two adsorption configurations of As(III/V) on the {110} facet (S1 and S2 in Fig. S9) and three configurations on the {214} facet (S1-S3 in Fig. S9) were studied, due to different distances of adjacent Fe atoms on these two facets (Fig. S2).

The comparison of E_{ads} values revealed that the favorable ^{2}C As(III/V) complex was resided at an Fe–Fe distance of 3.53 Å on the {110} facet, and the E_{ads} was estimated to be -2.57 eV for As(III) and -2.23 eV for As(V). On the {214} facet, the most favorable As(III/V) complex was located at an Fe–Fe distance of 3.52 Å, and the E_{ads} was calcualted to be -1.55 eV and -2.96 eV for As(III) and As(V) adsorption, respectively. By comparing E_{ads} values, the favorable active sites for As(III/V) adsorption are identified, which are one Fe_{3c} site on the {001} facet, two Fe_{5c} sites at an Fe–Fe distance of 3.53 Å on the {110} facet, and Fe_{3c} and Fe_{5c} sites at an Fe–Fe distance of 3.52 Å on the {214} facet.

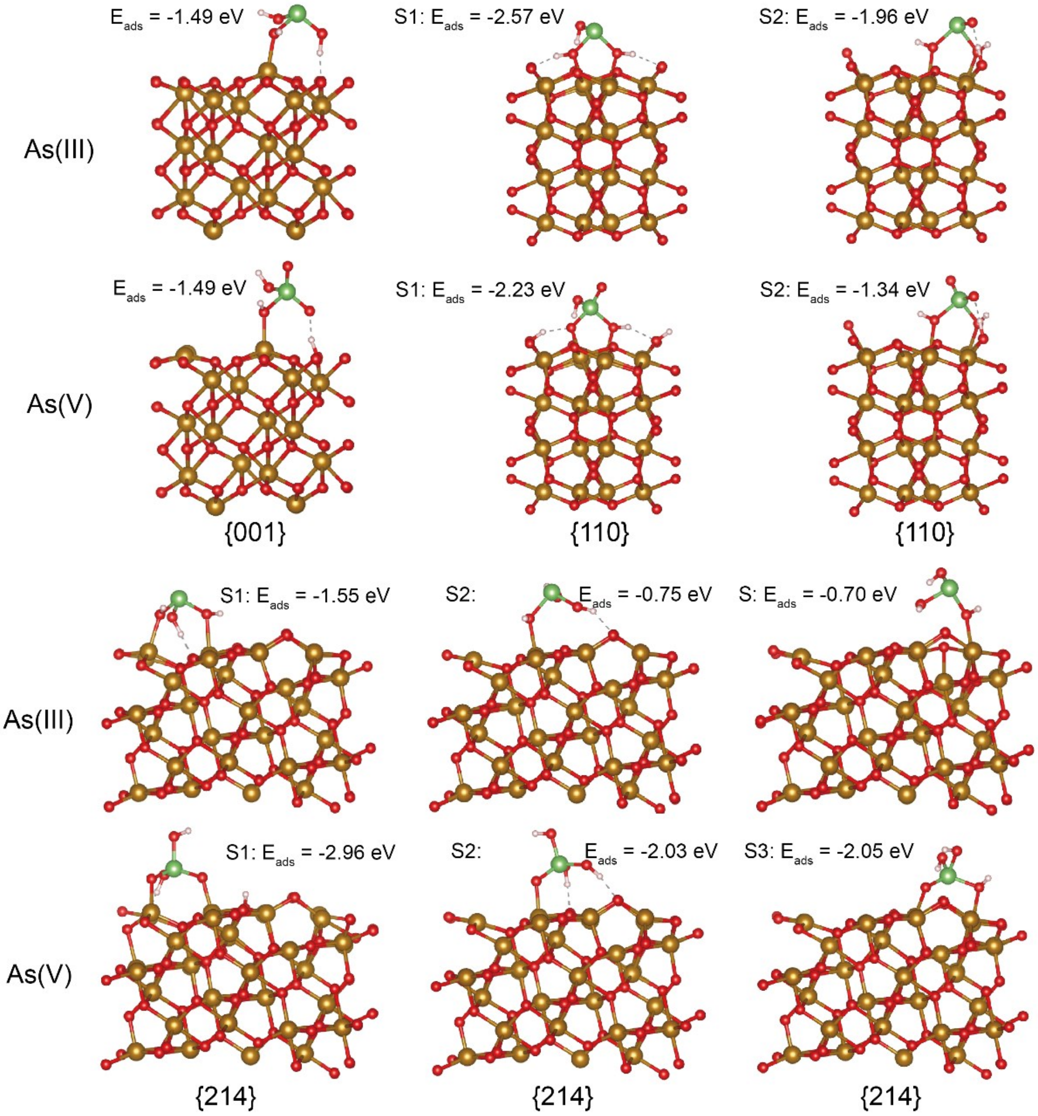

Fig. S9. DFT-optimized As(III/V) adsorption configurations on {001}, {110}, and {214} facets, the E_{ads} was calculated in Table S6.

Table S6. As(III/V) adsorption energies (eV) on Fe_2O_3 {001}, {110}, and {214} facets.

Facet	Structure	As(III)+slab	Slab	As(III)	E_{ads}
{001}	{001}-As(III)	-551.96	-514.22	-36.25	-1.49
{110}	{110}-As(III)-S1	-557.77	-518.95	-36.25	-2.57
	{110}-As(III)-S2	-557.16	-518.95	-36.25	-1.96
{214}	{214}-As(III)-S1	-806.13	-768.323	-36.25	-1.55
	{214}-As(III)-S2	-805.33	-768.323	-36.25	-0.75
	{214}-As(III)-S3	-805.27	-768.323	-36.25	-0.70

Facet		As(V)+slab	Slab	As(V)	E_{ads}
{001}	{001}-As(V)	-557.74	-514.22	-42.03	-1.49
{110}	{110}-As(V)-S1	-563.20	-518.95	-42.03	-2.23
	{110}-As(V)-S2	-562.31	-518.95	-42.03	-1.34
{214}	{214}-As(V)-S1	-813.31	-768.323	-42.03	-2.96
	{214}-As(V)-S2	-812.38	-768.323	-42.03	-2.03
	{214}-As(V)-S3	-812.40	-768.323	-42.03	-2.05

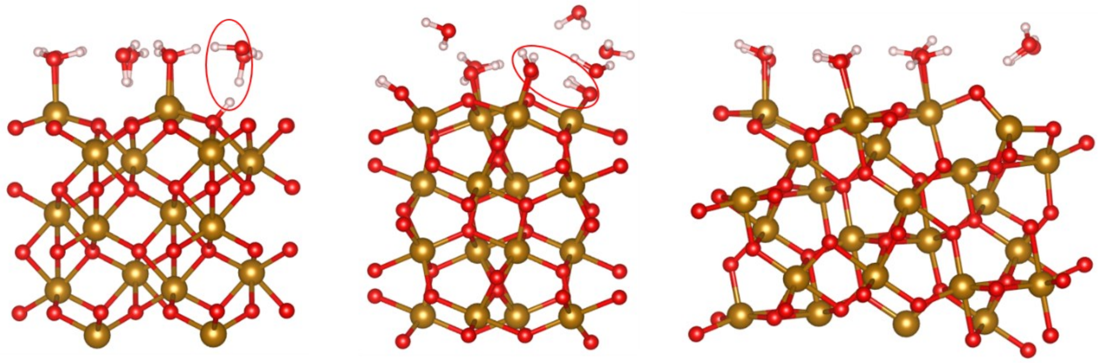

{001}-hydrated
γ = 0.86 J/m^2

{110}-hydrated
γ = 0.60 J/m^2

{214}-hydrated
γ = 1.44 J/m^2

Fig. S10. DFT-optimized geometry of water molecules adsorption on {001}, {110}, and {214} facets, the surface energy (γ) was calculated in Table S8. The red circles refer to the dissociative adsorption of water molecule.

Table S7. Adsorption energies (eV) of water molecule on Fe_2O_3 {001}, {110}, and {214} facets, as well as As(III/V) adsorption reaction and reaction energy in the water model.

Facets	Slab+8H_2O	Slab	H_2O	Number	E_{ads} (per H_2O)
{001}	-636.35	-514.22	-14.22	8	-1.05
{110}	-639.82	-518.95	-14.22	8	-0.89
{214}	-887.59	-768.32	-14.22	8	-0.69

Adsorption reactions and reaction energy calculation

{001}-As(III)	$[(Fe_{32}O_{48})(H_2O)_8]+ H_3AsO_3 \rightarrow [(Fe_{32}O_{48})(H_2O)_6]\text{-}H_3AsO_3 + 2H_2O$ $E_{rect} = 1.07$ eV
{001}-As(V)	$[(Fe_{32}O_{48})(H_2O)_8]+ H_3AsO_4 \rightarrow [(Fe_{32}O_{48})(H_2O)_6]\text{-}H_3AsO_4 + 2H_2O$ $E_{rect} = 0.97$ eV
{110}-As(III)	$[(Fe_{32}O_{48})(H_2O)_8]+ H_3AsO_3 \rightarrow [(Fe_{32}O_{48})(H_2O)_6]\text{-}H_3AsO_3 + 2H_2O$ $E_{rect} = -0.73$ eV
{110}-As(V)	$[(Fe_{32}O_{48})(H_2O)_8]+ H_3AsO_4 \rightarrow [(Fe_{32}O_{48})(H_2O)_6]\text{-}H_3AsO_4 + 2H_2O$ $E_{rect} = -0.53$ eV
{214}-As(III)	$[(Fe_{48}O_{72})(H_2O)_8]+ H_3AsO_3 \rightarrow [(Fe_{48}O_{72})(H_2O)_6]\text{-}H_3AsO_3 + 2H_2O$ $E_{rect} = -0.68$ eV
{214}-As(V)	$[(Fe_{48}O_{72})(H_2O)_8]+ H_3AsO_4 \rightarrow [(Fe_{48}O_{72})(H_2O)_6]\text{-}H_3AsO_4 + 2H_2O$ $E_{rect} = -1.27$ eV

Table S8. DFT calculated surface energy (γ) for hydrated surfaces.

Facet	E_{slab} (eV)	E_{bulk} (eV)	$E_{molecule}$ (eV)	*A* (Å^2)	γ (J/m^2)
{001}	-636.35 ($Fe_{32}O_{48}$+8H_2O)	-199.53 ($Fe_{12}O_{18}$)	-14.22	87.82	0.86
{110}	-639.82 ($Fe_{32}O_{48}$+8H_2O)			79.81	0.60
{214}	-887.59 ($Fe_{48}O_{72}$+8H_2O)			135.18	1.44

Table S9. Comparison of bond length for As(III/V) complexes on hydrated and bare surfaces.

	Bare surfaces			Hydrated surfaces		
	Bond	Distance (Å)	Average (Å)	Bond	Distance (Å)	Average (Å)
{001}-As(III)	As84-O49	1.81	1.83	As105-O55	1.82	1.85
	As84-O50	1.96		As105-O56	2.04	
	As84-O51	1.73		As105-O57	1.71	
	Fe65-O50	2.05	2.05	Fe71-O56	2.11	2.11
	Fe65-As84	3.52	3.52	Fe71-As105	3.43	3.43
{001}-As(V)	As85-O49	1.79	1.76	As106-O55	1.80	1.75
	As85-O50	1.65		As106-O56	1.65	
	As85-O51	1.92		As106-O57	1.86	
	As85-O52	1.67		As106-O58	1.69	
	Fe66-O51	2.02	2.02	Fe72-O57	2.06	2.06
	Fe66-As85	3.50	3.50	Fe72-As106	3.55	3.55
{110}-As(III)	As84-O49	1.75	1.84	As105-O55	1.79	1.83
	As84-O50	1.87		As105-O56	1.78	
	As84-O51	1.89		As105-O57	1.92	
	Fe57-O50	2.02	2.03	Fe63-O56	1.97	2.03
	Fe71-O51	2.04		Fe77-O57	2.08	
	Fe57-As84	3.42	3.45	Fe63-As105	3.30	3.42
	Fe71-As84	3.49		Fe77-As105	3.53	
{110}-As(V)	As85-O49	1.75	1.75	As106-O55	1.76	1.75
	As85-O50	1.75		As106-O56	1.74	
	As85-O51	1.88		As106-O57	1.86	
	As85-O52	1.63		As106-O58	1.64	
	Fe58-O50	1.93	1.98	Fe64-O56	2.00	2.05
	Fe72-O51	2.03		Fe78-O57	2.10	
	Fe58-As85	3.25	3.34	Fe64-As106	3.26	3.35
	Fe72-As85	3.43		Fe78-As106	3.44	
{214}-As(III)	As124-O73	1.85	1.83	As145-O79	1.92	1.84
	As124-O74	1.74		As145-O80	1.70	
	As124-O75	1.89		As145-O81	1.90	
	Fe87-O75	2.14	2.21	Fe93-O81	2.08	2.12
	Fe105-O73	2.28		Fe111-O79	2.17	
	Fe87-As124	3.66	3.64	Fe93-As145	3.53	3.67
	Fe105-As124	3.62		Fe111-As145	3.80	
{214}-As(V)	As125-O73	1.75	1.73	As146-O79	1.77	1.73
	As125-O74	1.72		As146-O80	1.68	
	As125-O75	1.74		As146-O81	1.77	
	As125-O76	1.70		As146-O82	1.69	
	Fe88-O74	1.91	1.95	Fe94-O80	2.03	2.03
	Fe106-O76	2.00		Fe112-O82	2.03	
	Fe88-As125	3.13	3.19	Fe94-As146	3.29	3.29
	Fe106-As125	3.24		Fe112-As146	3.30	

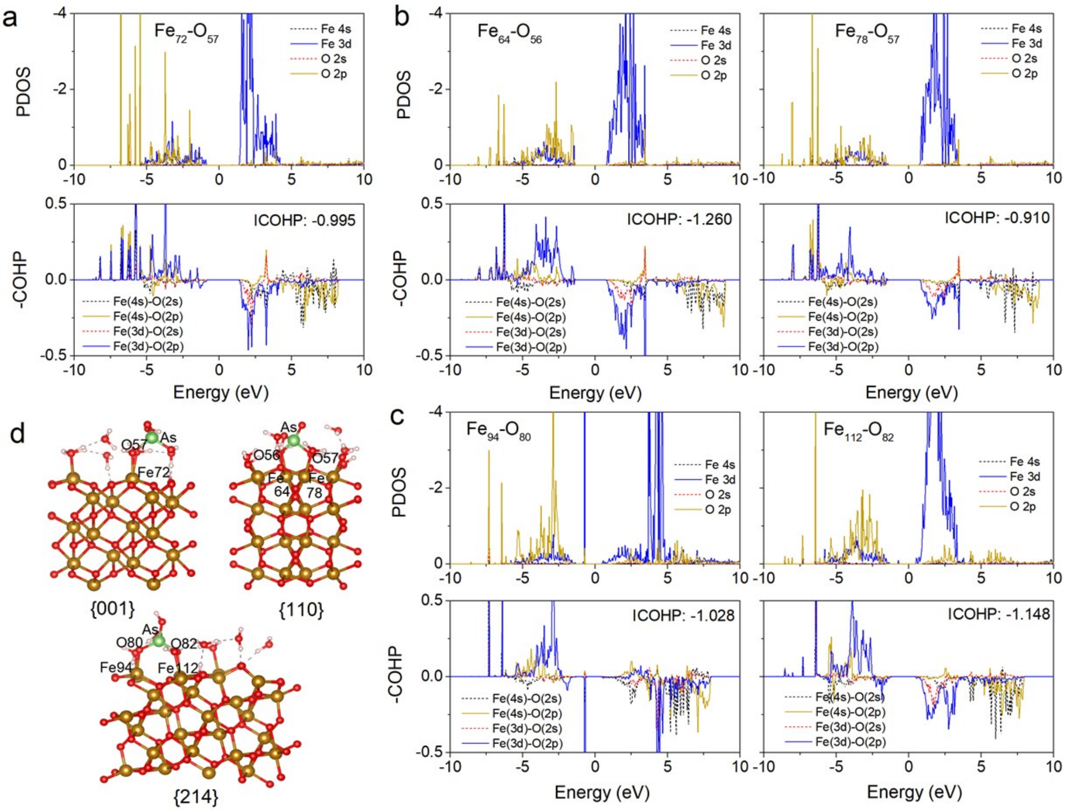

Fig. S11. PDOS (up panel) and –COHP (bottom panel) plots of the Fe–O bonds in As(V) complex on hydrated (a) {001}, (b) {110}, and (c) {214} facets. (d) DFT-optimized As(V) adsorption configurations on Fe_2O_3 facets. The red, brown, green, and white spheres represent O, Fe, As, and H atoms, respectively.

Table S10. Analysis of bond length and ICOHP for As(III/V) complexes on hydrated Fe_2O_3 facets.

Structure	Bond	Atom	Atom	Distance (Å)	ICOHP (eV)
{001}-As(III)	1	As105	O55	1.82	-3.079
	2	As105	O56	2.04	-1.736
	3	As105	O57	1.71	-4.065
	4	Fe71	O56	2.11	-0.889
{001}-As(V)	1	As106	O55	1.80	-3.228
	2	As106	O56	1.65	-5.053
	3	As106	O57	1.86	-2.680
	4	As106	O58	1.69	-4.376
	5	Fe72	O57	2.06	-0.995
{110}-As(III)	1	As105	O55	1.79	-3.387
	2	As105	O56	1.78	-3.480
	3	As105	O57	1.92	-2.364
	4	Fe63	O56	1.97	-1.394
	5	Fe77	O57	2.08	-0.994
{110}-As(V)	1	As106	O55	1.76	-3.586
	2	As106	O56	1.74	-3.870
	3	As106	O57	1.86	-2.737
	4	As106	O58	1.64	-5.313
	5	Fe64	O56	2.00	-1.260
	6	Fe78	O57	2.10	-0.910
{214}-As(III)	1	As145	O79	1.92	-2.379
	2	As145	O80	1.70	-4.171
	3	As145	O81	1.90	-2.462
	4	Fe93	O81	2.08	-0.893
	5	Fe111	O79	2.17	-0.772
{214}-As(V)	1	As146	O79	1.77	-3.534
	2	As146	O80	1.68	-4.543
	3	As146	O81	1.77	-3.548
	4	As146	O82	1.69	-4.392
	5	Fe94	O80	2.03	-1.028
	6	Fe112	O82	2.03	-1.148

Text S10. Chemical bonding analysis for As(III/V) adsorption on bare surfaces.

Fig. S12 shows the plots of the negative contributions of COHP (−COHP) versus energy (relative to E_{fermi}) for coordinated O and Fe atoms in As(III) complex on bare Fe_2O_3 facets. For As(III) adsorption, the bond length and integrated crystal orbital Hamilton population (ICOHP) for coordinated Fe_{57}–O_{50} (2.02 Å, -1.087 eV) and Fe_{71}–O_{51} (2.04 Å, -1.052 eV) on the {110} facet were comparable to Fe_{65}–O_{50} bond (2.05 Å, -1.030 eV) on the {001} facet (Table S11). The bond lengths and ICOHP for coordinated Fe_{87}–O_{75} (2.14 Å, -0.764 eV) and Fe_{105}–O_{73} (2.28 Å, -0.588 eV) on the {214} facet were observed. Similar bonding chemistry for As(V) adsorption was derived by analysis of bond length and ICOHP (Fig. S13), as evidenced by the coordinated Fe_{66}–O_{51} (2.02 Å, -1.072 eV) on {001} facet, Fe_{58}–O_{50} (1.93 Å, -1.545 eV) and Fe_{72}–O_{51} (2.03 Å, -1.088 eV) on {110} facet, and Fe_{88}–O_{74} (1.91 Å, -1.582 eV) and Fe_{106}–O_{76} (2.00 Å, -1.254 eV) on {214} facet (Table S11).

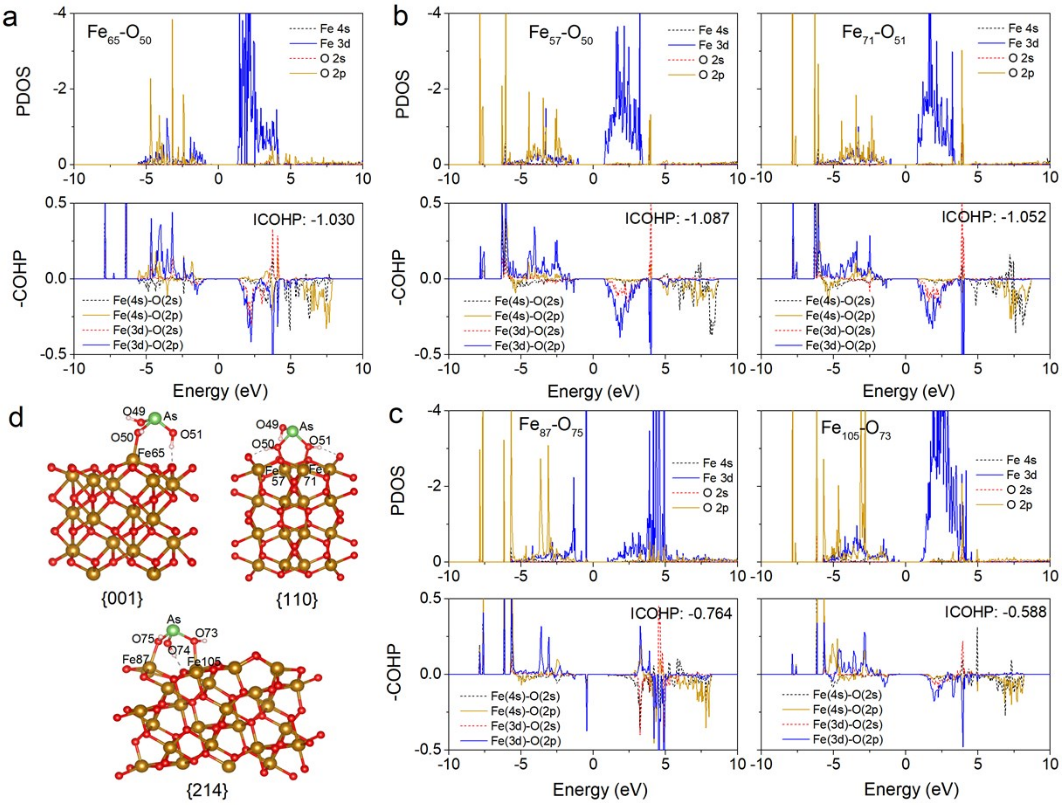

Fig. S12. PDOS (up panel) and –COHP (bottom panel) plots of the Fe–O bonds in As(III) complex on bare (a) {001}, (b) {110}, and (c) {214} facets. (d) DFT-optimized As(III) adsorption configurations on Fe_2O_3 facets. The red, brown, green, and white spheres represent O, Fe, As, and H atoms, respectively.

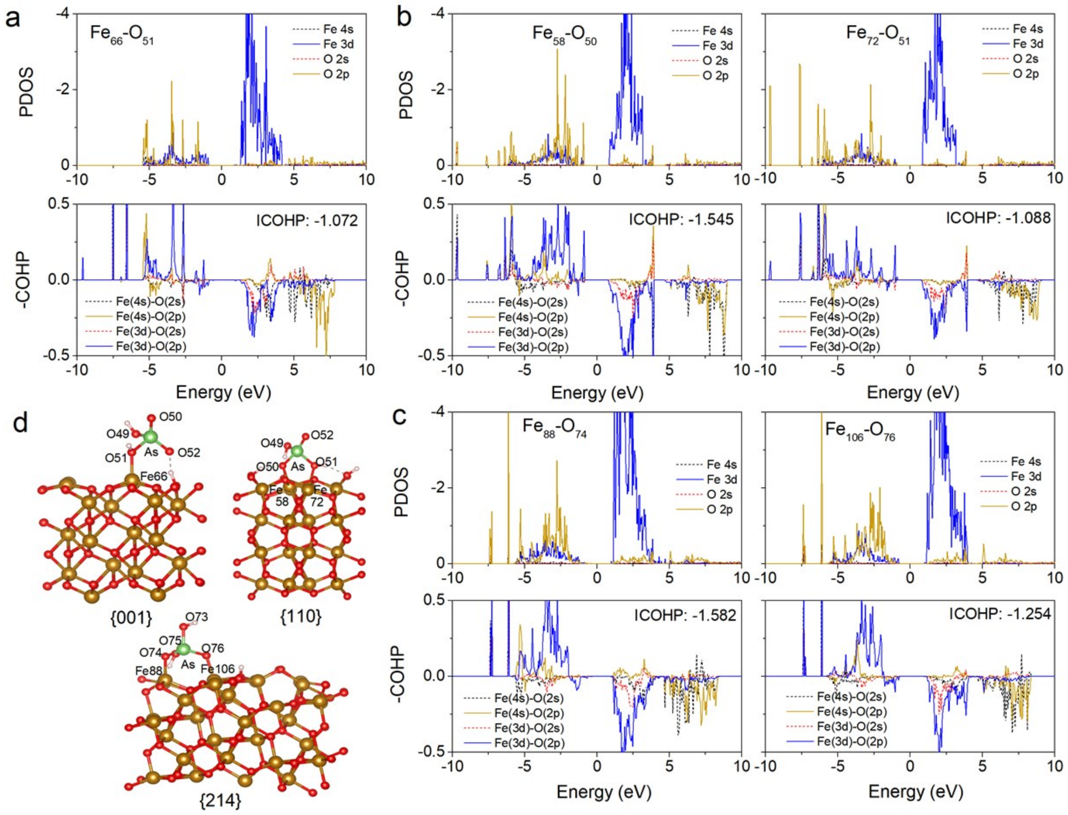

Fig. S13. PDOS (up panel) and –COHP (bottom panel) plots of the Fe–O bonds in As(V) complex on bare (a) {001}, (b) {110}, and (c) {214} facets. (d) DFT-optimized As(V) adsorption configurations on Fe_2O_3 facets. The red, brown, green, and white spheres represent O, Fe, As, and H atoms, respectively.

Table S11. Analysis of bond length and ICOHP for As(III/V) complexes on bare surfaces.

Structure	Bond	Atom	Atom	Distance (Å)	ICOHP (eV)
{001}-As(III)	1	As84	O49	1.81	-3.113
	2	As84	O50	1.96	-2.176
	3	As84	O51	1.73	-3.804
	4	Fe65	O50	2.05	-1.030
{001}-As(V)	1	As85	O49	1.79	-3.225
	2	As85	O50	1.65	-4.944
	3	As85	O51	1.92	-2.251
	4	As85	O52	1.67	-4.590
	5	Fe66	O51	2.02	-1.072
{110}-As(III)	1	As84	O49	1.75	-3.694
	2	As84	O50	1.87	-2.733
	3	As84	O51	1.89	-2.572
	4	Fe57	O50	2.02	-1.087
	5	Fe71	O51	2.04	-1.052
{110}-As(V)	1	As85	O49	1.75	-3.669
	2	As85	O50	1.75	-3.774
	3	As85	O51	1.88	-2.562
	4	As85	O52	1.63	-5.397
	5	Fe58	O50	1.93	-1.545
	6	Fe72	O51	2.03	-1.088
{214}-As(III)	1	As124	O73	1.85	-2.834
	2	As124	O74	1.74	-3.725
	3	As124	O75	1.89	-2.531
	4	Fe87	O75	2.14	-0.764
	5	Fe105	O73	2.28	-0.588
{214}-As(V)	1	As125	O73	1.75	-3.711
	2	As125	O74	1.72	-4.130
	3	As125	O75	1.74	-3.773
	4	As125	O76	1.70	-4.361
	5	Fe88	O74	1.91	-1.582
	6	Fe106	O76	2.00	-1.254

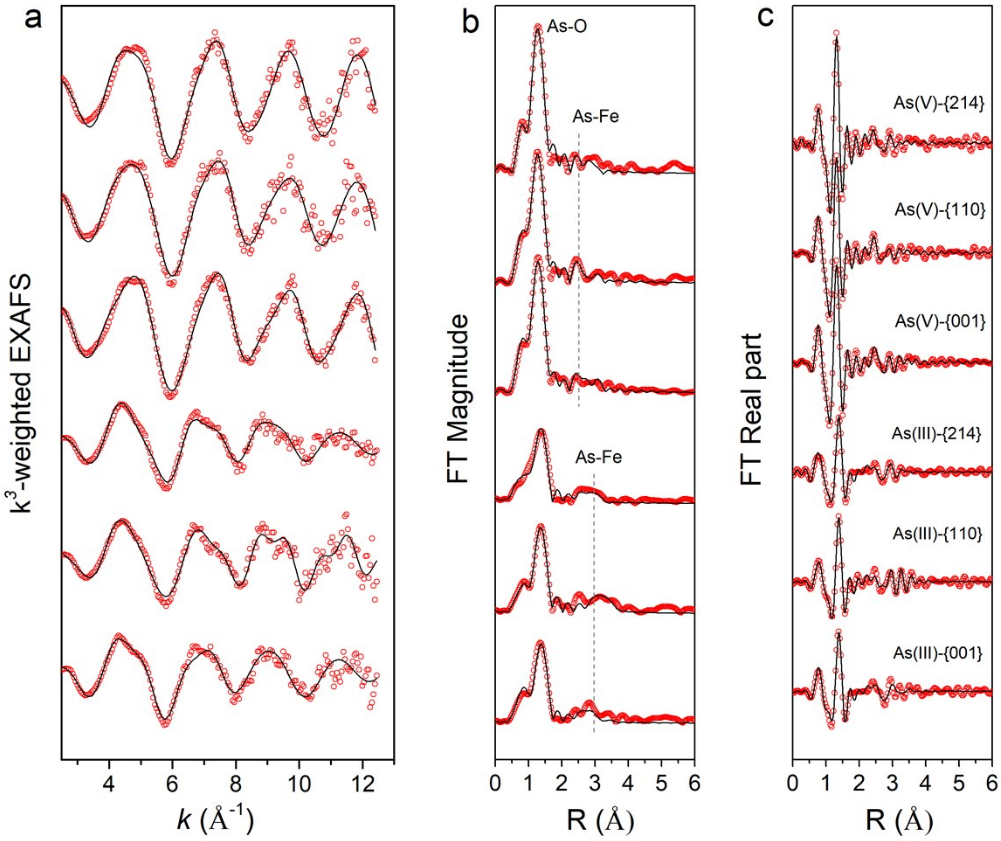

Fig. S14. (a) k^3-weighted As K-edge EXAFS spectra and their corresponding (b) FT magnitude and (c) real parts for As(III/V) adsorption on Fe_2O_3 {001}, {110}, and {214} facets. The samples were prepared by reacting 50 mg/L As(III/V) on 1 g/L Fe_2O_3 in 0.04 M NaCl at pH 7. The experimental and fitted data are shown as symbols and lines, respectively. The fitted parameters are presented in Table S12.

Table S12. As K-edge EXAFS fitting results of As(III/V) adsorption on Fe_2O_3 {001}, {110}, and {214} facets.

Sample	Path	CN	R(Å)	σ2(Å^2)	ΔE(eV)	R-factor
As(III)-{001}	As-O	2.9(3)	1.78(1)	0.003(2)	13.2(14)	0.039
	As-O-O	6	3.24	0.003		
	As-Fe	1	3.48(5)	0.010(8)		
As(III)-{110}	As-O	2.9(3)	1.77(1)	0.002(1)	8.5(17)	0.029
	As-O-O	6	3.10	0.002		
	As-Fe	1	3.36(4)	0.004(5)		
	As-Fe	1	3.64(5)	0.004(6)		
As(III)-{214}	As-O	3.0(3)	1.78(1)	0.004(2)	10.4(16)	0.038
	As-O-O	6	3.17	0.004		
	As-Fe	2	3.35(4)	0.013(6)		
As(V)-{001}	As-O	4.1(4)	1.69(1)	0.002(1)	7.4(12)	0.020
	As-O-O	12	3.15	0.002		
	As-Fe	1	3.27(5)	0.006(6)		
As(V)-{110}	As-O	4.2(4)	1.69(1)	0.002(1)	5.3(14)	0.025
	As-O-O	12	3.10	0.002		
	As-Fe	2	3.25(6)	0.014(8)		
As(V)-{214}	As-O	4.0(4)	1.68(1)	0.001(1)	3.4(19)	0.033
	As-O-O	12	3.08	0.001		
	As-Fe	2	3.29(6)	0.016(11)		

Parameter uncertainties in parentheses are given for the last significant figure; values without reported uncertainties were fixed during the fitting. R(Å): mean half path length. CN: coordination number. σ^2(Å^2): Debye-Waller factor. ΔE (eV): energy-shift parameter. $R\ factor = \sum_i (data_i - fit_i)^2 / \sum_i data$. The passive amplitude reduction factor, S_0^2, was fixed at 0.95.

Text S11. Chemical bonding analysis for hydrogen-bonding effect.

For As(III) complex on the {001} facet, the bond length of uncoordinated As$_{105}$–O$_{57}$ (1.71 Å) was shorter than that of uncoordinated As$_{105}$–O$_{55}$ (1.82 Å, Table S10). The shrink of As$_{105}$–O$_{57}$ bond was attributed to the deprotonation of As$_{105}$–O$_{57}$H by hydrogen-bonding interaction of H with surface O atoms (circle in Fig. S15). Similar hydrogen-bonding effect on As$_{8106}$–O$_{58}$H was resolved for As(V) complex on {001} facet, resulting in reduced bond length and increased ICOHP for deprotonated As$_{106}$–O$_{58}$ bond (1.69 Å, -4.376 eV) (Fig. S15, Table S10). The hydrogen-bonding effect facilitated As(III/V) molecules approaching to the surface, resulting in an As$_{105}$–Fe$_{71}$ distance of 3.43 Å for As(III) and As$_{106}$–Fe$_{72}$ distance of 3.55 Å for As(V) complexes.

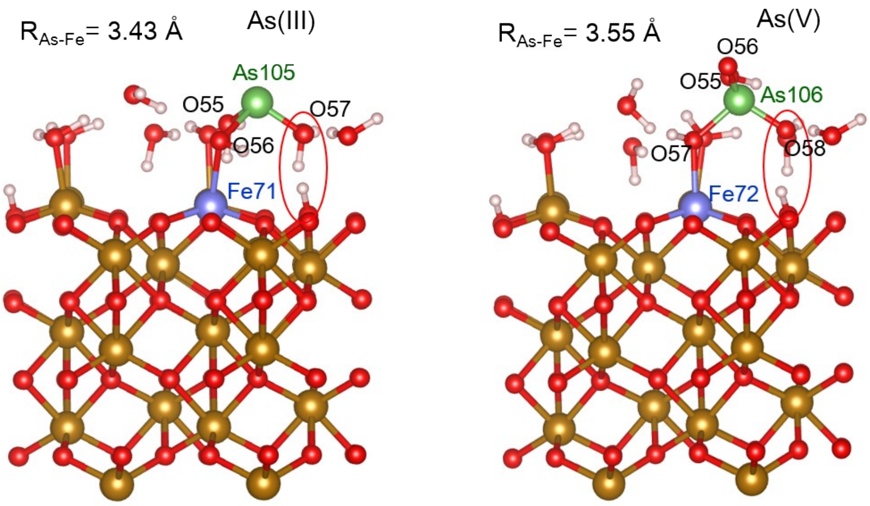

Fig. S15. DFT-optimized geometry of As(III) and As(V) adsorption on hydrated {001} facet. The red circles refer to the hydrogen-bonding effect.

References

1. R. J. Madix, The application of flash desorption spectroscopy to chemical reactions on surfaces: Temperature programmed reaction spectroscopy, *Crit. Rev. Solid State*, 1978, **7**, 143-152.
2. Y. Brechbuhl, I. Christl, E. J. Elzinga and R. Kretzschmar, Competitive sorption of carbonate and arsenic to hematite: Combined ATR-FTIR and batch experiments, *J. Colloid Interface Sci.*, 2012, **377**, 313-321.
3. S. E. Mason, C. R. Iceman, K. S. Tanwar, T. P. Trainor and A. M. Chaka, Pb(II) Adsorption on Isostructural Hydrated Alumina and Hematite (0001) Surfaces: A DFT Study, *J. Phys. Chem. C*, 2009, **113**, 2159-2170.
4. J. P. Perdew, K. Burke and M. Ernzerhof, Generalized gradient approximation made simple, *Phys. Rev. Lett.*, 1996, **77**, 3865-3868.
5. T. P. Trainor, A. M. Chaka, P. J. Eng, M. Newville, G. A. Waychunas, J. G. Catalano and G. E. Brown, Structure and reactivity of the hydrated hematite (0001) surface, *Surf. Sci.*, 2004, **573**, 204-224.
6. C. Liu, I. Tranca, R. A. van Santen, E. J. M. Hensen and E. A. Pidko, Scaling Relations for Acidity and Reactivity of Zeolites, *J. Phys. Chem. C*, 2017, **121**, 23520-23530.
7. R. Dronskowski and P. E. Blochl, Crystal Orbital Hamilton Populations (COHP): Energy-Resolved Visualization of Chemical Bonding in Solids Based on Density-Functional Calculations, *J. Phys. Chem.*, 1993, **97**, 8617-8624.
8. R. A. van Santen and I. Tranca, How molecular is the chemisorptive bond?, *Phys. Chem. Chem. Phys.*, 2016, **18**, 20868-20894.
9. V. Fung, Z. L. Wu and D. E. Jiang, New Bonding Model of Radical Adsorbate on Lattice Oxygen of Perovskites, *J. Phys. Chem. Lett.*, 2018, **9**, 6321-6325.
10. L. Yan, S. Hu, J. Duan and C. Jing, Insights from Arsenate Adsorption on Rutile (110): Grazing-Incidence X-ray Absorption Fine Structure Spectroscopy and DFT+U Study, *J. Phys. Chem. A*, 2014, **118**, 4759-4765.
11. S. E. Seo, M. Girard, M. O. de la Cruz and C. A. Mirkin, Non-Equilibrium Anisotropic Colloidal Single Crystal Growth with DNA, *Nat. Commun.*, 2018, **9**, 4558.
12. G. Wulff, On the Question of Speed of Growth and Dissolution of Crystal Surfaces, *Z. Kristallogr.*, 1901, **34**, 449-530.
13. Q. L. Yuan, P. F. Li, J. Liu, Y. Lin, Y. Y. Cai, Y. X. Ye and C. Liang, Facet-Dependent Selective Adsorption of Mn-Doped α-Fe_2O_3 Nanocrystals toward Heavy-Metal Ions, *Chem. Mater.*, 2017, **29**, 10198-10205.
14. S. Y. Cao, X. Zhang, X. P. Huang, S. H. Wan, X. Z. An, F. L. Jia and L. Z. Zhang, Insights into the facet-dependent adsorption of phenylarsonic acid on hematite nanocrystals, *Environ. Sci. Nano*, 2019, **6**, 3280-3291.
15. X. P. Huang, X. J. Hou, F. Wang, B. H. Guo, F. H. Song, L. Ling, J. C. Zhao and L. Z. Zhang, Molecular-scale structures of uranyl surface complexes on hematite facets, *Environ. Sci. Nano*, 2019, **6**, 892-903.
16. R. Gao, L. Pan, Z. Li, C. Shi, Y. Yao, X. Zhang and J.-J. Zou, Engineering Facets and Oxygen Vacancies over Hematite Single Crystal for Intensified Electrocatalytic H_2O_2 Production, *Adv. Funct. Mater.*, 2020, **30**.
17. X. Gong, J. You, J. Wang and L. Lu, Simulated and Experimental Raman Spectroscopic Studies on the Micro-Structure of Several Iron Compounds, *Spectrosc. Spect. Anal.*, 2018, **38**, 241-242.
18. C. Y. Cao, J. Qu, W. S. Yan, J. F. Zhu, Z. Y. Wu and W. G. Song, Low-Cost Synthesis of Flowerlike α-Fe_2O_3 Nanostructures for Heavy Metal Ion Removal: Adsorption Property and Mechanism, *Langmuir*, 2012, **28**, 4573-4579.
19. L.-S. Zhong, J.-S. Hu, H.-P. Liang, A.-M. Cao, W.-G. Song and L.-J. Wan, Self-assembled 3D flowerlike iron oxide nanostructures and their application in water treatment, *Adv. Mater.*, 2006, **18**, 2426-2431.
20. Z. Wei, R. Xing, X. Zhang, S. Liu, H. Yu and P. Li, Facile Template-Free Fabrication of Hollow Nestlike α-Fe_2O_3 Nanostructures for Water Treatment, *ACS Appl. Mater. Inter.*, 2013, **5**, 598-604.
21. X. T. Yang, L. Xia, J. L. Li, M. Dai, G. C. Yang and S. X. Song, Adsorption of As(III) on porous hematite synthesized from goethite concentrate, *Chemosphere*, 2017, **169**, 188-193.
22. K. Ramirez-Muniz, F. F. Jia and S. X. Song, Adsorption of As-V in aqueous solutions on porous hematite prepared by thermal modification of a siderite-goethite concentrate, *Environ. Chem.*,

2012, **9**, 512-520.

23. I. Carabante, J. Mouzon, J. Kumpiene, M. Gran, A. Fredriksson and J. Hedlund, Reutilization of Porous Sintered Hematite Bodies as Effective Adsorbents for Arsenic(V) Removal from Water, *Ind. Eng. Chem. Res.*, 2014, **53**, 12689-12696.
24. W. Y. Xu, B. Q. Yang, F. F. Jia, T. X. Chen, L. Yang and S. X. Song, Removal of As(V) from aqueous solution by using cement-porous hematite composite granules as adsorbent, *Results Phys.*, 2018, **11**, 23-29.
25. A. Majumder, L. Ramrakhiani, D. Mukherjee, U. Mishra, A. Halder, A. K. Mandal and S. Ghosh, Green synthesis of iron oxide nanoparticles for arsenic remediation in water and sludge utilization, *Clean Techno. Environ.*, 2019, **21**, 795-813.
26. Z. M. Liu, J. T. Chen, Y. C. Wu, Y. R. Li, J. Y. Zhao and P. Na, Synthesis of magnetic orderly mesoporous α-Fe_2O_3 nanocluster derived from MIL-100(Fe) for rapid and efficient arsenic(III,V) removal, *J. Hazard. Mater.*, 2018, **343**, 304-314.
27. W. S. Tang, Q. Li, S. A. Gao and J. K. Shang, Arsenic (III,V) removal from aqueous solution by ultrafine α-Fe_2O_3 nanoparticles synthesized from solvent thermal method, *J. Hazard. Mater.*, 2011, **192**, 131-138.
28. Y. C. Du, H. G. Fan, L. P. Wang, J. S. Wang, J. S. Wu and H. X. Dai, α-Fe_2O_3 nanowires deposited diatomite: highly efficient absorbents for the removal of arsenic, *J. Mater. Chem. A*, 2013, **1**, 7729-7737.
29. J. X. Wang, R. S. Yuan, L. Y. Xie, Q. F. Tian, S. Y. Zhu, Y. H. Hu, P. Liu, X. C. Shi and D. H. Wang, Photochemical treatment of As(III) with α-Fe_2O_3 synthesized from Jarosite Waste, *Rsc Adv.*, 2012, **2**, 1112-1118.
30. J. Gimenez, M. Martinez, J. de Pablo, M. Rovira and L. Duro, Arsenic sorption onto natural hematite, magnetite, and goethite, *J. Hazard. Mater.*, 2007, **141**, 575-580.
31. D. B. Singh, G. Prasad and D. C. Rupainwar, Adsorption technique for the treatment of As(V)-rich effluents, *Colloids Surf., A*, 1996, **111**, 49-56.
32. B. Prasad, C. Ghosh, A. Chakraborty, N. Bandyopadhyay and R. K. Ray, Adsorption of arsenite (As^{3+}) on nano-sized Fe_2O_3 waste powder from the steel industry, *Desalination*, 2011, **274**, 105-112.
33. S. Aredes, B. Klein and M. Pawlik, The removal of arsenic from water using natural iron oxide minerals, *J. Clean. Prod.*, 2012, **29-30**, 208-213.
34. Y. Jeong, M. Fan, S. Singh, C. L. Chuang, B. Saha and H. van Leeuwen, Evaluation of iron oxide and aluminum oxide as potential arsenic(V) adsorbents, *Chem. Eng. Process.*, 2007, **46**, 1030-1039.
35. Y. Mamindy-Pajany, C. Hurel, N. Marmier and M. Romeo, Arsenic (V) adsorption from aqueous solution onto goethite, hematite, magnetite and zero-valent iron: Effects of pH, concentration and reversibility, *Desalination*, 2011, **281**, 93-99.
36. D. Dickson, G. L. Liu and Y. Cai, Adsorption kinetics and isotherms of arsenite and arsenate on hematite nanoparticles and aggregates, *J. Environ. Manage.*, 2017, **186**, 261-267.
37. M. Dai, L. Xia, S. X. Song, C. S. Peng and A. Lopez-Valdivieso, Adsorption of As(V) inside the pores of porous hematite in water, *J. Hazard. Mater.*, 2016, **307**, 312-317.
38. Y. Wang, J. Lin, S. Wang, D. Zhang, F. Xiao, X. Wang and Y. Jia, Adsorption and transformation of thioarsenite at hematite/water interface under anaerobic condition in the presence of sulfide, *Chemosphere*, 2019, **222**, 422-430.
39. J. A. Sigrist and I. J. Burgess, ATR-IR spectroelectrochemical studies of arsenic speciation at the ferrihydrite-solution interface, *Can. J. Chem.*, 2019, **97**, 413-421.